Chemical and Structural Configuration of Pt Doped Metal Oxide Thin Films Prepared by Atomic Layer Deposition

Ranjith K. Ramachandran,*,[†] Matthias Filez,[‡,⊥] Eduardo Solano, [†,∇] Hilde Poelman, [‡] Matthias M. Minjauw,[†] Michiel Van Daele, [†] Ji-Yu Feng, [†] Andrea La Porta,[‖] Thomas Altantzis,[‖] Emiliano Fonda, [§] Alessandro Coati,[#] Yves Garreau,[#,^] Sara Bals,[‖] Guy B. Marin,[‡] Christophe Detavernier,[†] and Jolien Dendooven* ,[†]

[†]Conformal Coating of Nanostructures (CoCooN), Department of Solid State Sciences, Ghent University, Krijgslaan 281 (S1), 9000 Ghent, Belgium

[‡]Laboratory for Chemical Technology, Ghent University, Technologiepark 125, B-9052 Zwijnaarde, Belgium

[‖]Electron Microscopy for Materials Science (EMAT), University of Antwerp, Groenenborgerlaan 171, B-2020 Antwerp, Belgium

[§]SAMBA Beamline, [#]SixS Beamline, Synchrotron SOLEIL, L′Orme des Merisiers, Saint-Aubin, BP48, 91192 Gif-sur-Yvette, France, SOLEIL

[^]Université de Paris, Laboratoire Matériaux et Phénomènes Quantiques, CNRS, F-75013, Paris, France.

ABSTRACT: Pt doped semiconducting metal oxides and Pt metal clusters embedded in an oxide matrix are of interest for applications such as catalysis and gas sensing, energy storage and memory devices. Accurate tuning of the dopant level is crucial for adjusting the properties of these materials. Here, a novel atomic layer deposition (ALD) based method for doping Pt into In_2O_3 in specific, and metals in metal oxides in general, is demonstrated. This approach combines alternating exposures of Pt and In_2O_3 ALD processes in a single 'supercycle', followed by supercycle repetition leading to multilayered nanocomposites. The atomic level control of ALD and its conformal nature make the method suitable for accurate dopant control even on high surface area supports. Oxidation state, local structural environment and crystalline phase of the embedded Pt dopants were obtained by means of X-ray characterization methods and high angle annular dark-field scanning transmission electron microscopy (HAADF-STEM). In addition, this approach allows characterization of the nucleation stages of metal ALD processes, by stacking those states multiple times in an oxide matrix. Regardless of experimental conditions, a few Pt ALD cycles leads to the formation of oxidized Pt species due to their highly dispersed nature, as proven by X-ray absorption spectroscopy (XAS). Grazing-incidence small-angle X-ray scattering (GISAXS) and high-resolution scanning transmission electron microscopy, combined with energy dispersive X-ray spectroscopy (HR-STEM/EDXS) show that Pt is evenly distributed in the In_2O_3 metal oxide matrix without the formation of clusters. For a larger number of Pt ALD cycles, typ. > 10, the oxidation state gradually evolves towards fully metallic, and metallic Pt clusters are obtained within the In_2O_3 metal oxide matrix. This work reveals how tuning of the ALD supercycle approach for Pt doping allows controlled engineering of the Pt compositional and structural configuration within a metal oxide matrix.

INTRODUCTION

Metal oxides have been attracting great attention in various fields such as gas sensing, energy storage and catalytic applications. Adding noble metals to metal oxides is an effective way to improve the electronic properties of the oxides. Depending on how the addition takes place, either as atomically dispersed doping or as embedded nanoparticles (NPs) inside the metal oxide matrix, the resulting materials find their own unique applications. For example, metallic NPs embedded in metal oxides are widely used as charge storage materials in single electron memory devices.[1,2] On the other hand, noble metal doped semiconducting metal oxides (SMOs), such as $Pd-SnO_2$ and $Pt-In_2O_3$, have been found to outperform the undoped parent oxides in their catalytic and gas sensing properties.[3–6]

Discrete nanocrystal memory[1] has revolutionized the field of non-volatile memory devices (NVM), due to its high operation speed and scalability. Among nanocrystal materials, metal NPs are considered highly promising because of a better lateral isolation of each storage site and high density of states.[1] For charge storage in NVM devices,[1] NPs such as Pt, Ag and Au, embedded in dielectric layers, have been used, out of which Pt has been explored extensively.[7–13] In a metal based single electron transistor, the metal NPs are separated from the gate material by a thin layer of dielectric.[2] In order to accomplish better device performance, an adequate fabrication method, which can precisely control the NPs' size and surface areal density, as well as the dielectric thickness, is highly important. One technique that can fulfill this requirement is atomic layer deposition (ALD).[14] ALD is a vapour phase deposition technique that relies on sequential, self-limiting surface reactions, which enable a conformal deposition of the materials on complex 3D morphologies.[15] Recently, Orak et al. demonstrated the use of ALD for the successful deposition of ultra-small Pt NPs, as a charge trapping layer in thin film flash memory devices.[11]

It is well known that the sensing ability of SMOs can be greatly enhanced by noble metal doping. Pt doped In_2O_3 is one of the most interesting candidates among noble metal-doped SMOs. Pt doping in In_2O_3 sensors improves their performance in terms of sensitivity, response and recovery time.[3] Inyawilert et al.[4] successfully synthesized Pt doped In_2O_3 nanoparticles by single-step flame spray pyrolysis and found that 0.5 wt% Pt doping in In_2O_3 nanoparticles gave a significant enhancement towards NO_2 sensing along with a remarkable NO_2 selectivity amidst NO, H_2S, C_2H_5OH, and H_2. Pt doped In_2O_3 composites, synthesized by Rui-Juan et al. using an impregnation method, showed excellent formaldehyde sensing performance,[5] with 1 at% $Pt-In_2O_3$ composites having the best sensing performance.

Recently, Liu *et al.*[6] prepared mesoporous nanofibers of Pt loaded In_2O_3 by electrospinning and subsequent reduction. They found that Pt enhanced the sensing performance towards NO_2 down to ppb level, which was attributed to the chemical sensitization and catalytic properties of well-dispersed Pt NPs.

The aforementioned performance enhancement relies on the fact that the sensitivity of a SMO gas sensor is determined by the efficiency of the catalytic reactions that occur on its surface with the gas under detection.[16,17] Noble metals, being highly efficient catalysts, can enhance the reactions on gas sensor surfaces[17] by 1) decreasing the activation energy of those sensing reactions,[18,19] 2) increasing the electron transfer rate[20] and 3) providing more specific adsorption sites for oxygen,[21–25] all of which are beneficial to the gas sensing performance.[26] These in turn depend on the atomic level distribution and electronic state of the noble metal dopant in SMOs. Therefore, it is crucial to have synthesis methods that can precisely control the compositional and structural configuration of the dopant. Even though Pt doping in In_2O_3 using different methods has frequently been reported,[3–6,27,28] there are few reports focusing on the control of the exact chemical and structural nature of Pt within the oxide matrix. ALD, one of the techniques that offer atomic level control on material deposition, can be used as a potential tool in this regard.

Noble metal ALD on metal oxide surfaces often follows a nucleation controlled growth mechanism and results in the formation of nanoparticles during the early stages of the growth,[29,30] which has been a topic of interest in the recent years. For example, Pt ALD using $MeCpPtMe_3$ and O_2 gas has been extensively investigated,[30–36] which follows a combustion type reaction mechanism and results in the formation of Pt NPs during the initial cycles.[30,37] As the ALD process proceeds, the Pt NPs grow by different mechanisms such as NP nucleation, diffusion of adatoms and coalescence.[33,34] It is also demonstrated that during Pt ALD the reactant pulse (O_2 or O_3) leaves behind PtO_x species[31,32] on the surface, which enable the NP growth through Ostwald ripening. [38]Recently, Dendooven *et al.* demonstrated how the size and morphology of Pt nanoparticles can be tuned by combining different Pt ALD processes using different reactants.[36] The island growth mode in Pt ALD has been widely exploited for the synthesis of well-dispersed noble metal nanoparticles for applications such as catalysis and gas sensing. Researchers have also demonstrated the effective use of ALD for the synthesis of doped metal oxides[39–42] and metal NPs embedded in an oxide matrix.[43,44]

In this paper, we report an efficient way of preparing both noble metal (Pt) doped In_2O_3 thin films as well as In_2O_3 thin films with embedded Pt NPs, using a supercycle ALD approach. **Figure 1** demonstrates the basic principle of the synthesis method. Pt/In_2O_3 films with different Pt loadings were deposited on planar Si substrates covered with native SiO_2 (SiO_2/Si) substrates using different supercycles. Each supercycle consists of n_1 cycles of In_2O_3 and n_2 cycles of Pt ALD, and the supercycle is repeated n times such that the total number of Pt ALD cycles ($n*n_2$) remains the same for all samples. The resulting samples of Pt embedded in an In_2O_3 matrix are characterized chemically and structurally using a variety of X-ray based techniques, such as X-ray fluorescence (XRF), X-ray diffraction (XRD), X-ray absorption spectroscopy (XAS), Grazing-Incidence Small-Angle X-ray scattering (GISAXS) and High Angle Annular Dark Field Scanning Transmission Electron Microscopy (HAADF-STEM), combined with Energy Dis-

persive X-ray Spectroscopy (EDXS). In addition to giving valuable information on the dopant distribution and its chemical state, which provides strategies for fine-tuning the properties of doped metal oxides, the information obtained from these techniques also yields unique insight in the nucleation stage of Pt ALD.
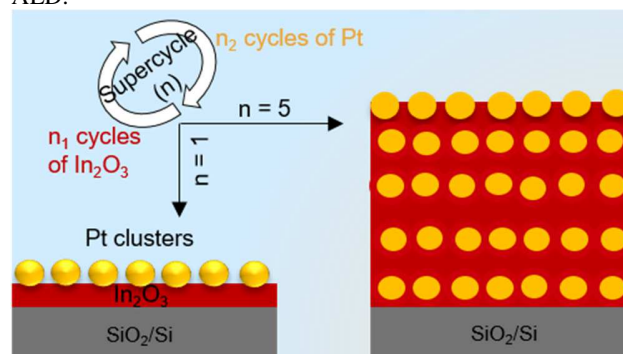

Figure 1. Schematic outline of the supercycle ALD approach for the controlled doping of Pt into the In_2O_3 matrix.

EXPERIMENTAL

ALD synthesis: All depositions were performed at 150 °C, in a home-built cold-wall ALD chamber.[45,46] In_2O_3 and Pt were deposited using alternating exposures of $In(TMHD)_3$ (99 %, Strem Chemicals) and O_2 plasma for In_2O_3 ALD[47] and $(MeCp)PtMe_3$ (99 %, Strem Chemicals) and O_3 for Pt ALD.[29,48] Ar with 99.999 % purity was used as a carrier gas for all precursors. O_3 was produced from a 99 % O_2/N_2 mixture with an AC-2025 (IN USA Inc.) generator, resulting in an O_3 concentration of 200 μg/ml. A typical In_2O_3 ALD cycle lasted 20 s with 5 s pulse time for both the precursor and reactant, and 5 s pumping after each pulse.[47] For Pt ALD, a static exposure mode was applied during both ALD reactions, resulting in a total cycle time of 50 s.[29,48,49]

Material characterization: XRR and XRD measurements were performed using a Bruker D8 diffractometer[50,51] with Cu Kα radiation. XRF measurements were performed using a Bruker Artax system with a Mo X-ray source (at an angle of 45° with the sample surface) and a silicon drift detector placed at an angle of 52° with the sample surface. The fluorescence signal was integrated over a period of 100 s. XAS measurements were performed at the SAMBA beamline of the SOLEIL synchrotron (Saint-Aubin, France) operating at 450 mA. All experiments were performed in fluorescence mode at the Pt L_{III} edge (E = 11564 eV) using a 35-element Ge detector (Canberra). A Pt foil and PtO_2 powder pellet were used for reference measurement in transmission mode, to prevent self-absorption. XAS data reduction and analysis were executed with the Demeter 0.9.13 software package by following the methodology of Koningsberger *et al.*[52]

GISAXS measurements were performed at the SixS beamline of the SOLEIL synchrotron. The samples were irradiated with 12.0 keV X-rays at an incidence angle of 0.5°. The 2D GISAXS patterns were acquired with a Dectris Eiger 1M detector, positioned at a distance of approximately 1.05 m from the sample, with an acquisition time of 60 s.

Cross-sectional samples for HAADF-STEM were prepared by an initial mechanical polishing, using an Allied Multiprep system with diamond-lapping films, down to a thickness of approximately 20 μm, followed by Ar+ ion milling by using a Leica EM RES102 apparatus, with acceleration voltages up to

4 kV and incident beam angles between 6° and 11°. Low and high magnification HAADF-STEM images and EDXS elemental maps were acquired using an aberration corrected cubed FEI Titan electron microscope operated at 300 kV, equipped with the ChemiSTEM system.[53] A probe convergence semi-angle and a detector collection inner semi-angle of 21 mrad and 55 mrad, respectively, were used for image acquisition.

RESULTS

Two series of samples have been prepared (**Table 1**): in series A, the number of Pt ALD cycles in the supercycle was limited to $n_2 = 1$, while varying the number of In_2O_3 cycles n_1 from 1 to 30, theoretically resulting in In_2O_3 thicknesses of 0.14 to 4.2 Å, based on the In_2O_3 growth per cycle of 0.14 Å. In series B, the number of Pt ALD cycles n_2 was varied from 1 to 30, while keeping the number of In_2O_3 cycles n_1 at 30. For all depositions, the value of n was chosen so that the total number of Pt ALD cycles equals 60, i.e. $n*n_2 = 60$. The total thickness and the composition (Pt at%) of the films were determined by using an XRF based calibration curve (**Figure S1**). While the next sections discuss a profound investigation of the Pt structure and chemical nature within the composite films, it is worth mentioning that the In XRF counts obtained for the resulting samples were in accord with the total number of In_2O_3 cycles, suggesting the absence possible influence of Pt on In_2O_3 ALD growth, in contrast to previous detailed research on the nucleation of Al_2O_3 ALD on Pt where an enhanced growth was observed during very first cycles.[54]

Table 1. Sample details. The error value in the brackets shows the standard deviation in the Pt at% across 3x4 cm² sample determined by performing XRF measurements across 5 points.

	Sample	Supercycle (n_1 In_2O_3 + n_2 Pt)*n	Total thickness (nm)	Pt at%
Series A	A1	(30 + 1) * 60	27.5	1.9 (± 0.2)
	A2	(20 + 1) * 60	19.4	2.5 (± 0.3)
	A3	(10 + 1) * 60	11.7	6.8 (± 0.7)
	A4	(5 + 1) * 60	8.4	18.3 (± 1.7)
	A5	(1 + 1) * 60	7.2	59.4 (± 2.8)
Series B	B1	(30 + 1) * 60	27.5	1.9 (± 0.2)
	B2	(30 + 2) * 30	15.9	4.9 (± 0.7)
	B3	(30 + 4) * 15	11.1	16.4 (± 1.6)
	B4	(30 + 10) * 6	7.7	27.6 (± 1.6)
	B5	(30 + 20) * 3	6.3	59.9 (± 3.0)
	B6	(30 + 30) * 2	6.4	70.7 (± 3.1)

The crystalline nature of the samples was examined using XRD. **Figure 2a** and **2b** show the XRD patterns of the samples in series A and B respectively. In both series, the diffraction peaks corresponding to In_2O_3 (222) (PDF 44-1087) are not visible for the samples with very low amount of In (i.e. high at% of Pt: sample A5, B4 –B6), since it lies below the XRD detection limit. In series A an intense diffraction peak corresponding metallic Pt (111) (PDF 87-0646) is observed for the sample with only 1 In_2O_3 ALD cycles (A5). The intensity of the metallic Pt peak decreased with increasing number of In_2O_3 ALD cycles,

disappearing from 10 In_2O_3 ALD cycles onwards. In series B, for only a few Pt ALD cycles, the XRD patterns show no peaks corresponding to metallic Pt (**Figure 2b**). The Pt peak starts to appear from 4 Pt ALD cycles onwards, indicating the presence of crystalline metallic Pt with increasing number of Pt ALD cycles. The nature of Pt for the samples with low at% Pt remains to be resolved as there are no Pt diffraction peaks visible: does this indicate the absence of crystalline Pt or is it just below the XRD detection limit? To answer this question, XAS measurements were performed at the Pt L_{III} edge.

In **Figure 3a**, the X-ray absorption near edge structure (XANES) spectra of the multilayer samples in series A are depicted together with the spectra of bulk $Pt^{(0)}$ and $Pt^{(+IV)}O_2$ references. The absorption edge of samples A1 – A3 are very close to each other and above oxidised Pt. As the number of In_2O_3 cycles decreases, the Pt edge energy shifts downward. In addition to the edge position, the white line height (WLH) (**Figure 3b**) provides a measure for the density of unoccupied $5d_{5/2}$ states to which $2p_{3/2}$ core-electrons are excited, and thus for the oxidation state of Pt. The WLH of samples A1 - A3 exceeds the one of PtO_2, showing that the Pt 5d valence band is strongly depleted in valence electrons compared to Pt in PtO_2. This implies that electron withdrawal from Pt by the In oxide surrounding is more significant compared to Pt in PtO_2, in accord with previous reports of Pt-doped SnO_2 oxides.[55] A steady decrease in the WLH of Pt is then observed for the samples A4 and A5, evolving to an oxidation state close to metallic Pt for sample A5. **Figure 3b** shows the evolution of the white line height of Pt as extracted from XANES, which indicates that for a supercycle comprising only a single Pt ALD cycle, the WLH of Pt increases from WLH_{Pt} to beyond WLH_{PtO2}, with an increasing number of In_2O_3 cycles. As the number of In_2O_3 reaches 10, Pt is maximally oxidized. For the samples with 5 In_2O_3 ALD cycles, XANES shows the presence of oxidised Pt, while the XRD measurement shows the presence of peaks corresponding to metallic Pt (**Figure 2a**). These results suggest the existence of metallic Pt clusters with an oxidised outer surface.

Complementary extended X-ray absorption fine structure (EXAFS) data allow a structural refinement of the local environment around Pt (**Figure 3c**). Qualitative analysis of the spectra for samples A1 – A3 shows peaks corresponding to the Pt-O bond. The absence of clear peaks in the higher R range indicates their atomically dispersed and disordered nature, which explains the absence of XRD peaks corresponding to Pt oxides in these samples (**Figure 2a**). With even less In_2O_3 cycles, the Pt-O amplitude decreases, with a subtle, but significant appearance of Pt-Pt peaks (A4). Finally, a complete depletion of Pt-O bonds occurs for sample A5, along with the appearance of a strong Pt fcc structure (R > 3 Å). Quantitative analysis of the EXAFS data with a Pt–Pt and Pt–O shell yields good agreement with the experimental signal (**Figure 3d**), which reveals that the Pt-Pt coordination number (N_{Pt-Pt}) is 0 for the samples with 30 – 10 In_2O_3 ALD cycles (A1 –A3), indicating no Pt cluster formation. For samples A4 and A5 the Pt-Pt coordination number steadily increases, showing that more pronounced Pt cluster formation is occurring with decreasing number of In_2O_3 cycles. These observations are in full accord with the results obtained from XRD measurements (**Figure 2a**).

Similarly, the XAS measurements for series B corroborate the observations made by the XRD measurements that no metallic clusters are formed for a low number of Pt ALD cycles and cluster formation is initiated for an increasing number of Pt ALD cycles per supercycle. The XANES spectra (**Figure 4a**)
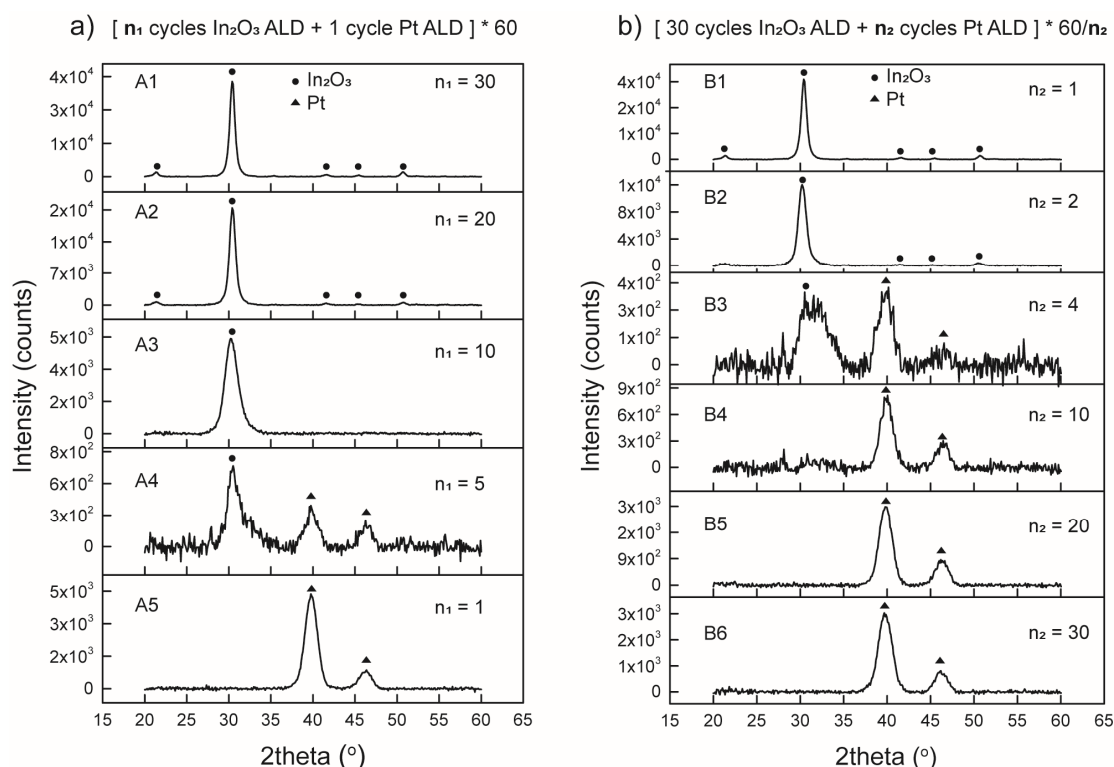
Figure 2. (**a**, **b**) XRD patterns of the samples in series A and B.

clearly show the presence of highly $5d_{5/2}$ electron depleted, oxidised Pt up to 2 Pt ALD cycles per supercycle, as indicated by their WLH which is higher than PtO_2. The WLH then gradually decreases with increasing number of Pt ALD cycles and the oxidation state Pt reaches 0 as the number of Pt cycles reaches 20, which fully agrees with the observations made by Filez *et al.*.[32] For the samples with 4 and 10 Pt ALD cycles, the combined data from XANES and XRD suggest the existence of metallic Pt clusters with an oxidised outer surface, leading to both Pt fcc Bragg diffractions in Figure 2b as well as an average oxidation state intermediate to Pt and PtO_2. Particularly, with increasing number of Pt cycles per supercycle, this oxidized surface fraction decreases, resulting in a decreasing average Pt oxidation state observed in XANES. Qualitative analysis of the EXAFS spectra (**Figure 4c**) shows peaks corresponding to Pt-O bonds only for the samples with 1 and 2 Pt ALD cycles, which then diminish as the Pt-Pt bond becomes more prominent with increasing number of Pt ALD cycles. A quantitative analysis of the data further confirms this observation, as can be seen in **Figure 4d**.

The particle morphology and cluster evolution were characterized by GISAXS measurements. The acquired GISAXS patterns for samples in series A and B are shown in **Figure 5a** and **b**, respectively. The number of scattering minima and maxima along q_z, at $q_y = 0$ nm^{-1}, is directly related to the thickness of the samples, with the highest number of minima and maxima for the thickest layers as measured by XRF. More interestingly, the presence of a scattering maximum along the q_y direction indicates the formation of Pt clusters in the film.[36] In series A, there are extra scattering peaks visible along the q_y direction, when

the number of In_2O_3 cycles is below 10. This appearance indicates that the Pt deposited in subsequent ALD supercycles interact with each other and form clusters. For more than 10 cycles of In_2O_3, the deposited Pt species get coated and covered by In_2O_3, effectively burying them and preventing interaction with Pt species deposited during the next supercycle. In the case of series B, the patterns clearly reveal that Pt cluster formation occurs with increasing number of Pt ALD cycles. The interference maximum at $q_y \neq 0$ nm^{-1} is indicative of the presence of clusters in the films. The q_y-position of the maximum, $q_{y,max}$, provides an estimate of the average lateral distance between the clusters (center-to-center) by applying the $2\pi/q_{y,max}$ approximation.[36,56] **Figure S3a** and **b** show the horizontal line profiles taken at the q_z-position of the scattering maximum. **Figure 5c** and **d** display the $2\pi/q_{y,max}$ values extracted from these profiles as a function of the number of In_2O_3 and Pt ALD cycles per supercycle in series A and B, respectively. The analysis reveals a shorter center-to-center distance between the metallic Pt clusters in sample A4 (ca. 5.5 nm) than in sample A5 (ca. 7.0 nm). This together with the appearance of higher order interference maxima along q_z only for sample A5, suggests the presence of relatively smaller clusters in A4. Hence, already 5 ALD cycles of In_2O_3 (~0.7Å) partially prevent the Pt nuclei from interacting with each other, thus hindering their clustering. In series B, the center-to-center distance between the Pt nanoclusters increases with the number of Pt ALD cycles per supercycle. Knowing that the Pt loading also increases, this result indicates that larger clusters are formed when more Pt ALD cycles are applied, as expected. The increase in center-to-center distance with the number of Pt ALD cycles is in line with the results obtained by Dendooven *et al.*, who recorded GISAXS patterns as a function
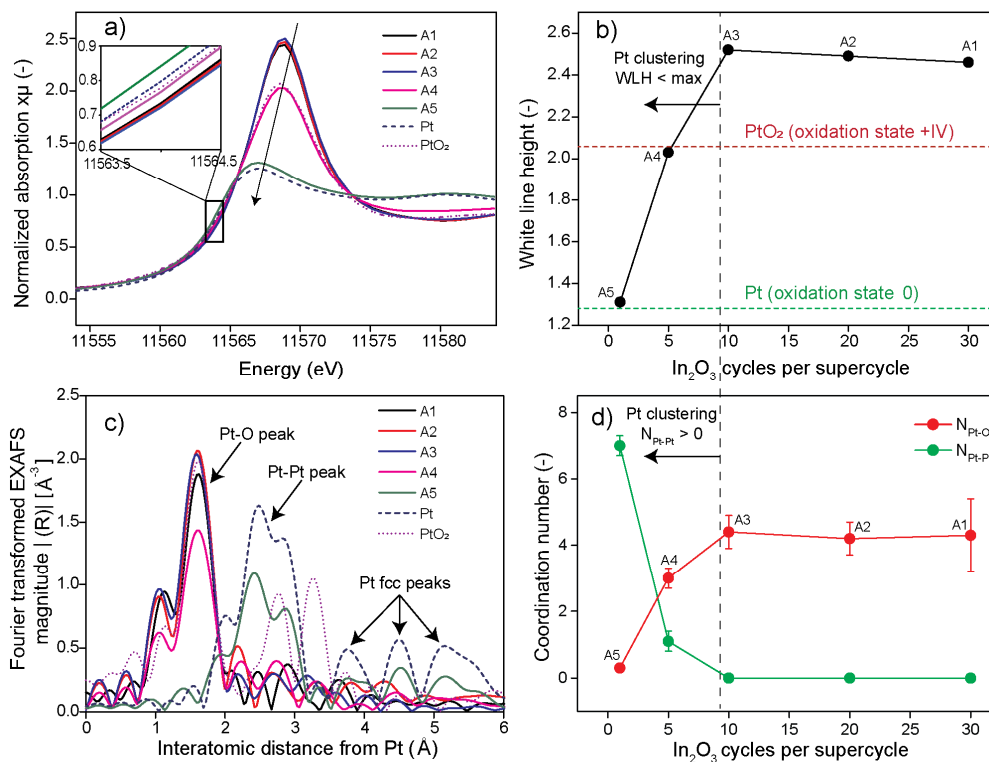
Figure 3. (**a**, **c**) XANES and k^2-weighted Fourier-transformed EXAFS magnitudes of the multilayer samples in series A. The reference signals from Pt and PtO_2 are shown as dashed and dotted lines, respectively. (**b**, **d**) The variation in WLH and the change in Pt-Pt and Pt-O coordination numbers with n_1, the number of In_2O_3 ALD cycles per supercycle, for 1 Pt ALD cycle.
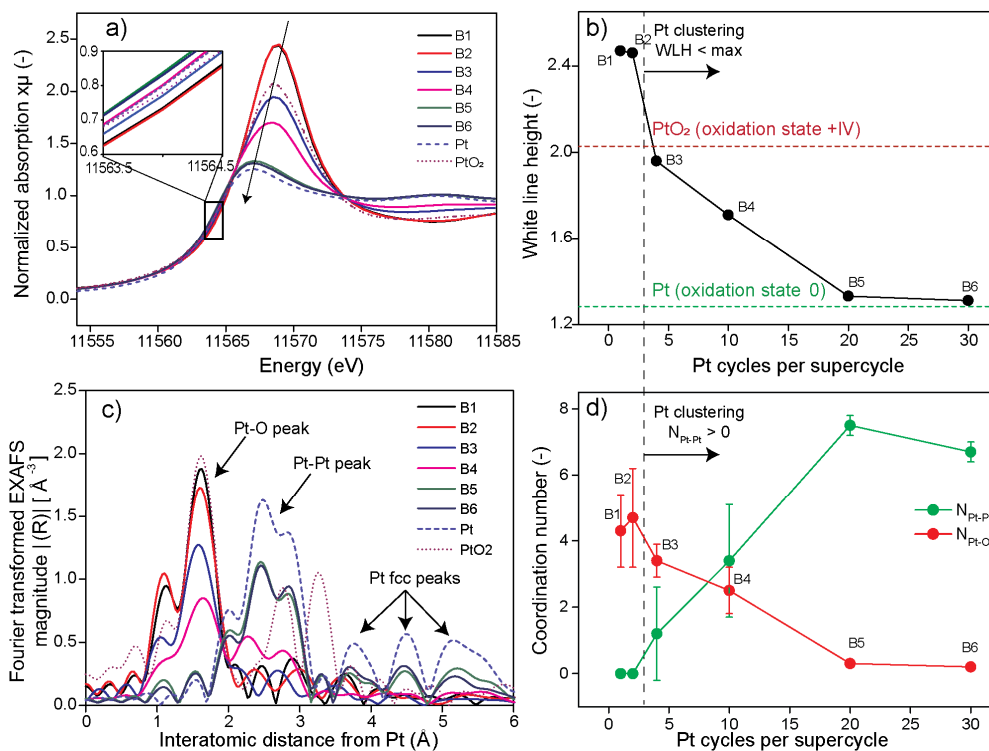

Figure 4. (**a**, **c**) XANES and k^2-weighted Fourier-transformed EXAFS magnitudes of the multilayer samples in series B. The reference signals from Pt and PtO_2 are shown as dashed and dotted lines, respectively. (**b**, **d**) The variation in WLH and the change in Pt-Pt and Pt-O coordination numbers with n_2, the number of Pt ALD cycles per supercycle, with 30 In_2O_3 ALD cycles.
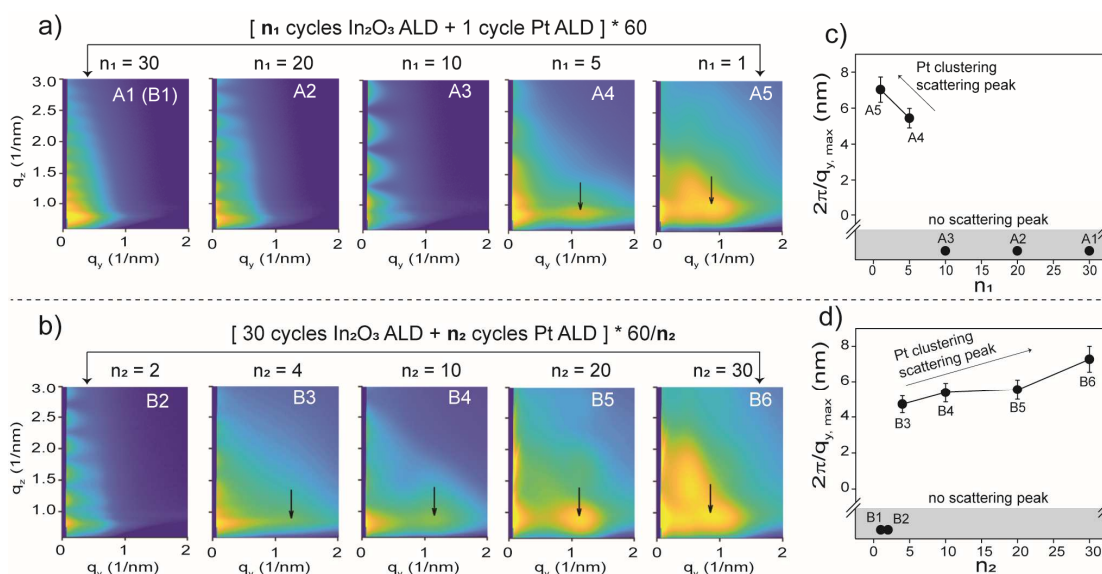
Figure 5. (**a**,**b**) Experimental 2D GISAXS patterns of Pt/In$_2$O$_3$ multilayer samples in series A and B. The arrows indicate the position of the relevant scattering maximum along the q$_y$ direction. (**c**,**d**) $2\pi/q_{y,max}$ value, as an approximation of the lateral inter-cluster distance, as a function of n$_1$ in series A (**c**) and n$_2$ in series B (**d**). Shaded parts in (**c**) and (**d**) indicate the region with no scattering peaks. Note that sample A1 and B1 are the same.

of the number of Pt ALD cycles with O$_2$ as co-reactant on a SiO$_2$ surface and observed a gradual increase in the inter-cluster distance.[36] Note that the ALD cycle number for which GISAXS indicates cluster formation in series A and B corresponds to the cycle number for cluster formation obtained from the XAS characterization.

To further confirm the formation of metallic Pt clusters versus uniform intermixing of oxidised Pt in the In$_2$O$_3$ matrix, two samples (B2 and B4) were selected for HR-STEM investigation, in which B2 is expected to have a uniform distribution of PtO$_x$ in the In$_2$O$_3$ matrix, while metallic Pt cluster formation is expected in the case of B4. As visible in the HAADF-STEM image (**Figure S4**), the thickness of each sample was uniform, approximately 16 and 8 nm for B2 and B4, respectively, which is in close agreement with the thickness estimated using the XRF calibration [**Table 1**]. HR-STEM images evident the absence of crystalline Pt clusters in sample B2, suggesting a uniform distribution of Pt throughout the In$_2$O$_3$ matrix (**Figure 6a**). The STEM image also confirms the presence of crystalline In$_2$O$_3$ (inset Fourier Transform (FT) pattern of **Figure 6a**). In the case of sample B4, metallic Pt clusters (inset of **Figure 6b**) surrounded by thin layers of In$_2$O$_3$ are observed with an average inter-cluster projected distance of *ca.* 5 nm (**Figure 6b**), which is in line with the result obtained from the GISAXS measurement. The EDXS elemental maps further corroborate the presence of a uniform mixture of Pt/In$_2$O$_3$ and metallic Pt clusters for sample B2 and B4, respectively. The quantification of the EDXS maps revealed a Pt at% of *ca.* 6.6 and 26.3 for samples B2 and B4 respectively, which is in accordance with the values obtained from XRF calibration.

Well-separated metallic Pt clusters, along the vertical direction, were obtained by depositing a thicker variant of sample B4 (B4-T), by increasing the number of In$_2$O$_3$ cycles to 120, while keeping the number of Pt ALD cycles the same [6*(120 cycles In$_2$O$_3$ + 10 cycles Pt)]. The HR-STEM image of the sample

(**Figure 6c**) clearly shows 6 layers of metallic Pt clusters embedded in an In$_2$O$_3$ matrix, with each layer separated by *ca.* 1.5 – 2 nm of In$_2$O$_3$, which is equal to the expected thickness of an In$_2$O$_3$ film resulting from 120 ALD cycles. This shows the capability of the presented method to fine-tune the vertical distance between embedded metallic clusters, simply by changing the number of ALD cycles of the oxide per supercycle, which is of great importance for applications such as metal based single electron memory devices.

DISCUSSION

The performance enhancement of (noble) metal doped metals oxides relies on a number of parameters such as size, composition, oxidation state and distance between the noble metal particles etc., depending on the envisioned applications. The proposed method enables controlled doping of Pt/PtO$_x$ species inside the In$_2$O$_3$ matrix with the ability to fine-tune their chemical and structural properties. Here, with the help of XRD and XAS, we show that by varying the number of either In$_2$O$_3$ (series A) or Pt (series B) ALD cycles in a supercycle, the oxidation state of the Pt dopant can be changed from +4 to 0. **Figure 7a** and **b** represent an overview of the results obtained from XRD, XRF and XAS analysis, for the samples in series A and B, respectively. **Figure 7a** shows that, for samples containing 1 Pt ALD cycle per supercycle, the Pt XRF counts (left Y-axis, green circles) decrease when more In$_2$O$_3$ cycles are incorporated. This is not surprising, as the Pt ALD process starts with a nucleation-controlled growth mode[29,57] and its growth occurs selectively on noble metals over oxides.[58,59] In a typical Pt ALD process on an oxide surface, nuclei are formed during the initial cycles, which enhance the growth during subsequent ALD cycles, until a steady state growth is achieved. Here, the In$_2$O$_3$ film grown in between and on top of the initial Pt deposits prevents the interaction with incoming precursor molecules during the next Pt ALD cycle, and thus delays the growth. The more In$_2$O$_3$ cycles
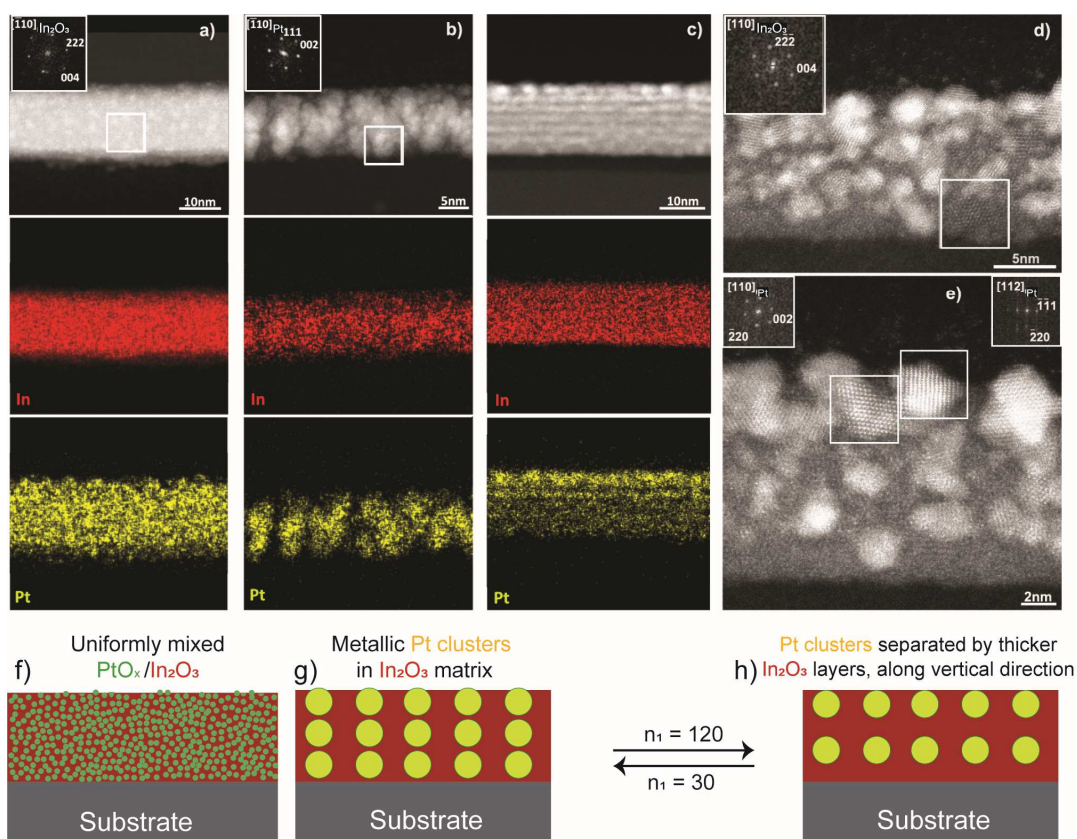
Figure 6. (**a**,**b**) HAADF-STEM images and the corresponding EDXS elemental maps of In and Pt for cross-sections of samples B2 and B4, respectively. From the Fourier Transform (FT) patterns, given as insets in figures 6a and b, which are obtained from the regions indicated by the white rectangles, the presence of crystalline In_2O_3 and Pt respectively is clear. (**c**) HAADF-STEM image and the corresponding EDXS elemental maps of In and Pt for sample B4-T and (**d**,**e**) high resolution HAADF-STEM images from different thin locations of sample B4-T, showing the presence of crystalline metallic Pt clusters (**e**) surrounded by crystalline In_2O_3 (**d**), indicated by the white rectangles. Schematic illustration of the structural configuration of (**f**) uniformly mixed PtO_x/In_2O_3, (**g**) metallic Pt clusters and (**h**) metallic Pt clusters with increased vertical spacing, as interpreted from STEM images.

are incorporated, the slower the observed growth of Pt, as suggested by the decrease in Pt XRF counts. The value of Pt XRF counts reaches a minimum with 10 In_2O_3 ALD cycles and stays constant afterwards, suggesting that 10 In_2O_3 ALD cycles (~1.4 Å thick In_2O_3 film) are enough to cover the initial nuclei completely, preventing their interaction with Pt deposited in the next supercycle and keeping them in their oxidized state (increased WHL, right Y-axis, blue circles) without the formation of metallic Pt clusters, as suggested by a decrease in the Pt (111) XRD peak intensity (left Y-axis, red circles) and the Pt-Pt coordination number (right Y-axis, orange circles).

In series B, the number of In_2O_3 cycles was set to 30, aiming to prevent major interaction between the Pt species deposited in subsequent supercycles. In these samples, an increase in the Pt XRF counts was observed with increasing number of Pt ALD cycles per supercycle (**Figure 7 b**), as expected. The figure also shows the shift from fully oxidized to metallic Pt, with increasing number of Pt ALD cycles, as revealed by an increase in the Pt (111) XRD peak intensity and Pt-Pt coordination number as well as a decrease in the WHL. This observation is in line with the results obtained by Filez et al., on the nucleation behavior of the O_3 based Pt ALD process,[32] where initial nucleation starts with the formation of PtO_x entities. As the number of ALD cycles increases, these PtO_x species interact with each other resulting in the formation of metallic Pt clusters.

In conclusion, for the samples with fully reduced Pt (0), high resolution HAADF-STEM, XRD and GISAXS together show the formation of metallic clusters embedded in an In_2O_3 matrix. On the other hand, a uniform mixture of dispersed PtO_x within crystalline In_2O_3 was obtained for samples with fully oxidised Pt. For samples A4, B3 and B4, XRD and XAS together suggest the formation of metallic Pt clusters with an oxidised outer surface. **Figure 7(c-e)** schematically represents the formation of different flavours of Pt species inside the In_2O_3 matrix, by changing the number of either Pt or In_2O_3 ALD cycles per supercycle. Thus, this method allows the controlled engineering of the Pt-In_2O_3 compositional and structural configuration, by adjusting the ALD supercycles. Further, this approach can also be extended for the synthesis of other metal-metal oxide systems, either by replacing In_2O_3 with other metal oxides or by replacing Pt with other noble metals such as Pd,[60] Ag[61] and Au,[62,63] where a nucleation controlled growth is observed.

In addition, this method paves a way for studying the nucleation stages of (noble) metal ALD processes, which is desirable for the synthesis of well-designed nanoparticles. Although Pt ALD using (MeCp)PtMe$_3$ and an oxidizing reactant has been investigated by several researchers, most of these studies focused on the steady growth rather than on the nucleation stages.[64–66] Moreover, they report mainly on the influence of either the chemical nature or crystalline state of the substrate[67–69]
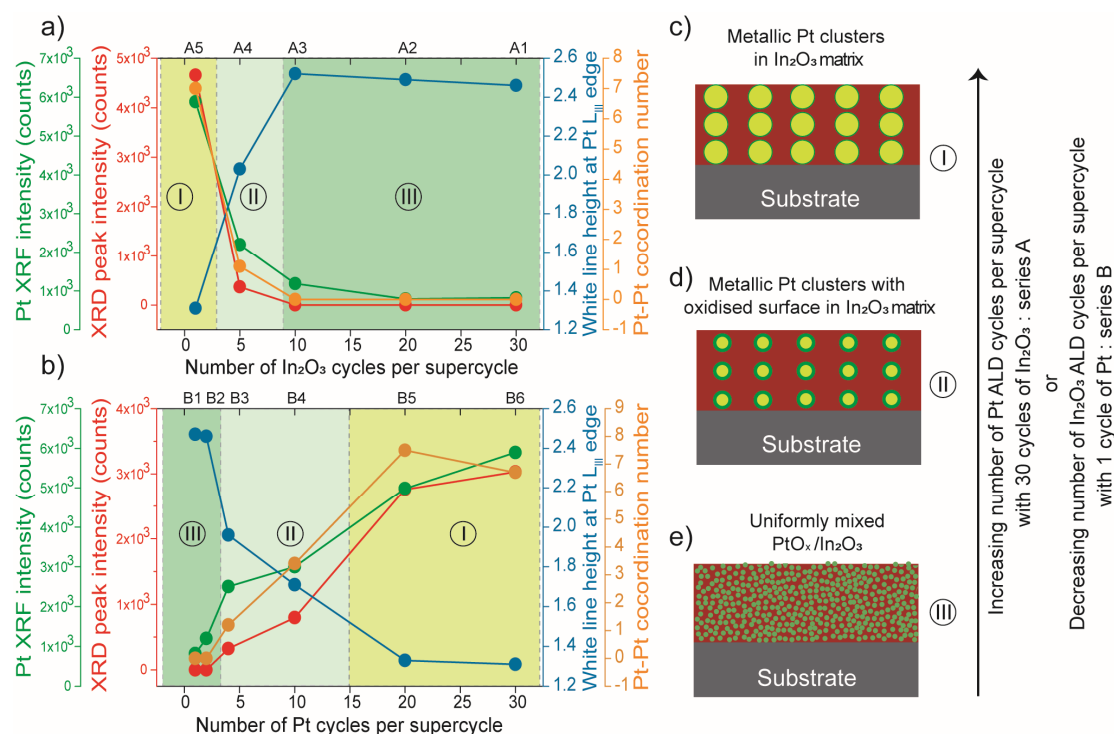
Figure 7. Variation of Pt XRF counts (green), Pt (111) XRD peak intensity (red), Pt L_{III} edge white line height (blue) and Pt-Pt coordination number (orange) with: (**a**) the number of In_2O_3 ALD cycles, per supercycle with 1 cycle of Pt ALD and (**b**) the number of Pt ALD cycles, per supercycle with 30 In_2O_3 ALD cycles. (**c-e**) Schematic illustration of the structural configuration of (**c**) uniformly mixed PtO_x/In_2O_3, (**d**) metallic Pt clusters with oxidised outer surface and (**h**) fully reduce metallic Pt clusters.

or the partial pressure[38] or the type of reactants[36], on the nucleation behaviour. Only a few studies have investigated the exact nature of Pt in the early nucleation stages, such as oxidation state, crystalline nature, size and dispersion of the platinum nanoparticles.[31,32]

Since the amount of growing material is very low, the investigation of the nucleation often demands the use of high surface area supports such as powders[31,70,71] or mesoporous silica[32] or the use of a dedicated complex set up to carry out *in situ* investigations.[32] Here comes in the advantage of the proposed multilayer approach: it enables such characterization on conventional planar silicon substrates, which are commonly used in the field of ALD. By performing the Pt and In_2O_3 ALD process sequentially, a particular nucleation stage in the Pt growth process can be preserved in a thin oxide matrix. By repeating the supercycle, a collection of this particular state can be obtained, which can provide a reasonable measurement signal. This makes characterization of even a single Pt ALD cycle feasible with techniques such as XAS, GISAXS, *etc.*. The XRD measurements together with the XAS results reveal the presence of highly oxidised dispersed PtO_x at the beginning of the ALD process, up to 2 Pt ALD cycles, which is in line with observations made by Christensen *et al.* on high surface area powder.[31] As the number of cycles increases, the oxidation state of Pt gradually decreases and results in the formation of larger species with a metallic Pt core surrounded by a PtO_x shell, as revealed by XRD and XAS measurements, respectively. Finally, with 20 Pt ALD cycles, fully reduced metallic Pt clusters are formed, which is in accord with the *in situ* nucleation study by Filez *et al.*.[32] The present study also reveals that interaction between the already deposited PtO_x nuclei and the subsequent Pt precursor pulse can be pre-

vented by coating the nuclei with a certain number of In_2O_3 cycles. This enables isolating particular nucleation stages of Pt in their as-deposited states. The formation of metallic clusters with increasing number of Pt ALD cycles, as well the prevention of cluster formation by applying In_2O_3 ALD cycles are confirmed with GISAXS measurements. HAADF-STEM measurements, combined with EDXS data further confirmed the uniform distribution of Pt in the In_2O_3 matrix during the initial nucleation stages and the formation of crystalline Pt with higher number of Pt ALD cycles.

CONCLUSION

This work demonstrates the controlled doping of Pt, both from a compositional and structural point of view, within a metal oxide matrix, using an ALD supercycle approach. Control over the average Pt oxidation state and Pt morphological nature (from uniform doping to embedded Pt clusters) is obtained by simply tuning the number of either In_2O_3 or Pt ALD cycles in a supercycle. A systematic study using advanced characterization methods, such as XRD, XAS, GISAXS and HAADF-STEM combined with EDXS, furnished detailed insight into the electronic state and structure of Pt dopants inside an In_2O_3 matrix. The investigations show that the oxidation state of Pt gradually shifted from +4 to 0 with increasing number of Pt ALD cycles. For only few Pt ALD cycles per supercycle, the PtO_x species are evenly distributed in the metal oxide matrix without the formation of clusters. For a larger number of Pt ALD cycles per surpercycle, fully reduced metallic Pt is obtained, in the form of Pt clusters. In addition, this multilayer approach allows characterization of the nucleation stages of metal ALD processes, by freezing those states through embedding and stacking them

multiple times. This allows use of XAS and other techniques to study even a single metal ALD cycle, without the need for the use of high surface area supports. In conclusion, this strategy opens up new opportunities for the controlled doping with metals, in general, and at the same time for the advanced study of nucleation stages of different (noble) metal ALD processes.

ASSOCIATED CONTENT

Supporting Information

The Supporting Information is available free of charge on the ACS Publications website.

Additional information on XRF based composition and thickness determination, Details of EXAFS analysis, Horizontal line profiles taken at the q_z-position of the main scattering maximum in the GISAXS patterns of the samples in series A and B, HAADF-STEM image showing the uniformity and thickness of sample B2 and B4 (PDF)

AUTHOR INFORMATION

Corresponding Author

*Email: Jolien.Dendooven@UGent.be
*Email: Ranjith.KaruparambilRamachandran@UGent.be

Present Addresses

$^\perp$Inorganic Chemistry and Catalysis Group, Debye Institute for Nanomaterials Science, Utrecht University, Universiteitsweg 99, 3584 CG Utrecht, The Netherlands.

$^\nabla$ALBA Synchrotron Light Source, NCD beamline, Carrer de la Llum 2-26, 08290 Cerdanyola del Vallès, Spain.

Author Contributions

The manuscript was written through contributions of all authors. All authors have given approval to the final version of the manuscript.

Notes

The authors declare no competing financial interest.

REFERENCES
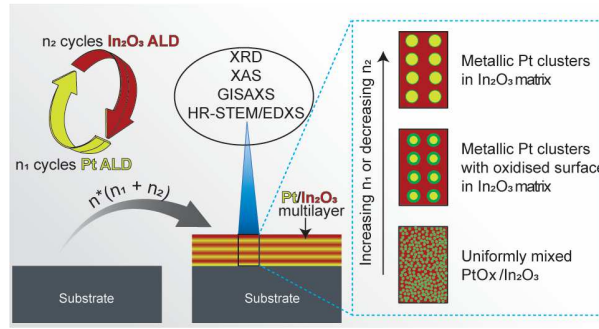
(1)   Chang, T. C.; Jian, F. Y.; Chen, S. C.; Tsai, Y. T. Developments in Nanocrystal Memory. *Mater. Today* **2011**, *14*, 608–615.

(2)   Chen, W.; Ahmed, H. Metal-Based Single Electron Transistors. *J. Vac. Sci. Technol. B Microelectron. Nanom. Struct.* **1997**, *15*, 1402.

(3)   Neri, G.; Bonavita, A.; Micali, G.; Rizzo, G.; Pinna, N.; Niederberger, M. In_2O_3 and $Pt-In_2O_3$ Nanopowders for Low Temperature Oxygen Sensors. *Sensors Actuators, B Chem.* **2007**, *127*, 455–462.

(4)   Inyawilert, K.; Channei, D.; Tamaekong, N.; Liewhiran, C.; Wisitsoraat, A.; Tuantranont, A.; Phanichphant, S. Pt-Doped In_2O_3 Nanoparticles Prepared by Flame Spray Pyrolysis for NO_2 Sensing. *J. Nanoparticle Res.* **2016**, *18*, 1–17.

(5)   Ma, R. J.; Zhao, X.; Zou, X.; Li, G. D. Enhanced Formaldehyde Sensing Performance at Ppb Level with Pt-Doped Nanosheet-Assembled In_2O_3 Hollow Microspheres. *J. Alloys Compd.* **2018**, *732*, 863–870.

(6)   Liu, Y.; Gao, X.; Li, F.; Lu, G.; Zhang, T.; Barsan, N. Pt-In_2O_3 Mesoporous Nanofibers with Enhanced Gas Sensing Performance towards Ppb-Level NO_2 at Room Temperature. *Sensors Actuators, B Chem.* **2018**, *260*, 927–936.

(7)   Zhou, G.; Wu, B.; Li, Z.; Xiao, Z.; Li, S.; Li, P. Memory Characteristics and Tunneling Mechanism of Pt Nano-Crystals Embedded in $HfAlO_x$ Films for Nonvolatile Flash Memory Devices. *Curr. Appl. Phys.* **2015**, *15*, 279–284.

(8)   Jeff, R. C.; Yun, M.; Ramalingam, B.; Lee, B.; Misra, V.; Triplett, G.; Gangopadhyay, S. Charge Storage Characteristics of Ultra-Small Pt Nanoparticle Embedded GaAs Based Non-Volatile Memory. *Appl. Phys. Lett.* **2011**, *99*, 2012–2015.

(9)   Mukherjee, S.; Zheng, H.; Gangopadhyay, K.; Gangopadhyay, S. Influence of Pt Nanoparticle Induced Defects and Surface Coverage in Determining Asymmetric Programming/Erasing Signatures for Nanocrystal Embedded Nonvolatile Memory Applications. *Adv. Mater. Interfaces* **2016**, *3*, 1–17.

(10)   Choi, H.; Choi, B. S.; Kim, T. W.; Jung, S. J.; Chang, M.; Lee, T.; Hwang, H. Memory Characteristics of a Self-Assembled Monolayer of Pt Nanoparticles as a Charge Trapping Layer. *Nanotechnology* **2008**, *19*.

(11)   Orak, İ.; Eren, H.; Bıyıklı, N.; Dâna, A. Utilizing Embedded Ultra-Small Pt Nanoparticles as Charge Trapping Layer in Flashristor Memory Cells. *Appl. Surf. Sci.* **2019**, *467–468*, 715–722.

(12)   Dufourcq, J.; Bodnar, S.; Gay, G.; Lafond, D.; Mur, P.; Molas, G.; Nieto, J. P.; Vandroux, L.; Jodin, L.; Gustavo, F.; et al. High Density Platinum Nanocrystals for Non-Volatile Memory Applications. *Appl. Phys. Lett.* **2008**, *92*, 2006–2009.

(13)   Novak, S.; Lee, B.; Yang, X.; Misra, V. Platinum Nanoparticles Grown by Atomic Layer Deposition for Charge Storage Memory Applications. *J. Electrochem. Soc.* **2010**, *157*, H589.

(14)   George, S. M. Atomic Layer Deposition: An Overview. *Chem. Rev* **2010**, *110*, 111–131.

(15)   Miikkulainen, V.; Leskelä, M.; Ritala, M.; Puurunen, R. L. Crystallinity of Inorganic Films Grown by Atomic Layer Deposition: Overview and General Trends. *J. Appl. Phys.* **2013**, *113*, 021301.

(16)   Müller, S. A.; Degler, D.; Feldmann, C.; Türk, M.; Moos, R.; Fink, K.; Studt, F.; Gerthsen, D.; Bârsan, N.; Grunwaldt, J. D. Exploiting Synergies in Catalysis and Gas Sensing Using Noble Metal-Loaded Oxide Composites. *ChemCatChem* **2018**, *10*, 864–880.

(17)   Wang, C.; Yin, L.; Zhang, L.; Xiang, D.; Gao, R. Metal Oxide Gas Sensors: Sensitivity and Influencing Factors. *Sensors* **2010**, *10*, 2088–2106.

(18)   Xing, R.; Li, Q.; Xia, L.; Song, J.; Xu, L.; Zhang, J.; Xie, Y.; Song, H. Au-Modified Three-Dimensional In_2O_3 Inverse Opals: Synthesis and Improved Performance for Acetone Sensing toward Diagnosis of Diabetes. *Nanoscale* **2015**, *7*, 13051–13060.

(19)   Yildiz, A.; Crisan, D.; Dragan, N.; Iftimie, N.; Florea, D.; Mardare, D. Effect of Formaldehyde Gas Adsorption on the Electrical Conductivity of Pd-Doped TiO_2 Thin Films. *J. Mater. Sci. Mater. Electron.* **2011**, *22*, 1420–1425.

(20)   Tian, S.; Ding, X.; Zeng, D.; Wu, J.; Zhang, S.; Xie, C. A Low Temperature Gas Sensor Based on Pd-Functionalized Mesoporous SnO_2 Fibers for Detecting Trace Formaldehyde.

RSC Adv. **2013**, *3*, 11823–11831.

(21) Wang, S.; Xiao, B.; Yang, T.; Wang, P.; Xiao, C.; Li, Z.; Zhao, R.; Zhang, M. Enhanced HCHO Gas Sensing Properties by Ag-Loaded Sunflower-like In_2O_3 Hierarchical Nanostructures. *J. Mater. Chem. A* **2014**, *2*, 6598–6604.

(22) Bai, S.; Liu, H.; Sun, J.; Tian, Y.; Luo, R.; Li, D.; Chen, A. Mechanism of Enhancing the Formaldehyde Sensing Properties of Co_3O_4 via Ag Modification. *RSC Adv.* **2015**, *5*, 48619–48625.

(23) Lei, T.; Zhang, S.; Li, D.; Zhang, W.; Huang, S.; Xie, C. The Influence of Au and Pt Electrodes on the Stability of TiO_2 under UV Light Activation for Sensing Formaldehyde in Moisture Circumstances. *Sensors Actuators, B Chem.* **2014**, *199*, 15–21.

(24) Fang, F.; Bai, L.; Song, D.; Yang, H.; Sun, X.; Sun, H.; Zhu, J. Ag-Modified In_2O_3/ZnO Nanobundles with High Formaldehyde Gas-Sensing Performance. *Sensors (Switzerland)* **2015**, *15*, 20086–20096.

(25) Lin, Y.; Wei, W.; Li, Y.; Li, F.; Zhou, J.; Sun, D.; Chen, Y.; Ruan, S. Preparation of Pd Nanoparticle-Decorated Hollow SnO_2 Nanofibers and Their Enhanced Formaldehyde Sensing Properties. *J. Alloys Compd.* **2015**, *651*, 690–698.

(26) Liu, X.; Chen, N.; Han, B.; Xiao, X.; Chen, G.; Djerdj, I.; Wang, Y. Nanoparticle Cluster Gas Sensor: Pt Activated SnO_2 Nanoparticles for NH_3 Detection with Ultrahigh Sensitivity. *Nanoscale* **2015**, *7*, 14872–14880.

(27) Kim, S. S.; Park, J. Y.; Choi, S. W.; Kim, H. S.; Na, H. G.; Yang, J. C.; Kim, H. W. Significant Enhancement of the Sensing Characteristics of In_2O_3 Nanowires by Functionalization with Pt Nanoparticles. *Nanotechnology* **2010**, *21*.

(28) Selvakumar, D.; Dharmaraj, N.; Kumar, N. S.; Padaki, V. C. Oxygen Sensing Properties of Platinum Doped Indium Oxide Nanoparticles Prepared by Hydrothermal Method. *Synth. React. Inorganic, Met. Nano-Metal Chem.* **2015**, *45*, 753–758.

(29) Dendooven, J.; Ramachandran, R. K.; Devloo-Casier, K.; Rampelberg, G.; Filez, M.; Poelman, H.; Marin, G. B.; Fonda, E.; Detavernier, C. Low-Temperature Atomic Layer Deposition of Platinum Using (Methylcyclopentadienyl)-Trimethylplatinum and Ozone. *J. Phys. Chem. C* **2013**, *117*, 20557–20561.

(30) Baker, L.; Cavanagh, A. S.; Seghete, D.; George, S. M.; Mackus, A. J. M.; Kessels, W. M. M.; Liu, Z. Y.; Wagner, F. T. Nucleation and Growth of Pt Atomic Layer Deposition on Al_2O_3 Substrates Using (Methylcyclopentadienyl)-Trimethyl Platinum and O_2 Plasma. *J. Appl. Phys.* **2011**, *109*.

(31) Christensen, S. T.; Elam, J. W.; Rabuffetti, F. A; Ma, Q.; Weigand, S. J.; Lee, B.; Seifert, S.; Stair, P. C.; Poeppelmeier, K. R.; Hersam, M. C.; et al. Controlled Growth of Platinum Nanoparticles on Strontium Titanate Nanocubes by Atomic Layer Deposition. *Small* **2009**, *5*, 750–757.

(32) Filez, M.; Poelman, H.; Ramachandran, R. K.; Dendooven, J.; Devloo-Casier, K.; Fonda, E.; Detavernier, C.; Marin, G. B. In Situ XAS and XRF Study of Nanoparticle Nucleation during O_3-Based Pt Deposition. *Catal. Today* **2014**, *229*, 2–13.

(33) Grillo, F.; Van Bui, H.; La Zara, D.; Aarnink, A. A. I.; Kovalgin, A. Y.; Kooyman, P.; Kreutzer, M. T.; van Ommen, J. R. From Single Atoms to Nanoparticles: Autocatalysis and Metal Aggregation in Atomic Layer Deposition of Pt on TiO_2 Nanopowder. *Small* **2018**, *14*, 1–11.

(34) Grillo, F.; Van Bui, H.; Moulijn, J. A.; Kreutzer, M. T.; Van Ommen, J. R. Understanding and Controlling the Aggregative Growth of Platinum Nanoparticles in Atomic Layer Deposition: An Avenue to Size Selection. *J. Phys. Chem. Lett.* **2017**, *8*, 975–983.

(35) Mackus, A. J. M.; Weber, M. J.; Thissen, N. F. W.; Garcia-Alonso, D.; Vervuurt, R. H. J.; Assali, S.; Bol, A. A.; Verheijen, M. A.; Kessels, W. M. M. Atomic Layer Deposition of Pd and Pt Nanoparticles for Catalysis: On the

Mechanisms of Nanoparticle Formation. *Nanotechnology* **2016**, *27*, 034001.

(36) Dendooven, J.; Ramachandran, R. K.; Solano, E.; Kurttepeli, M.; Geerts, L.; Heremans, G.; Rongé, J.; Minjauw, M. M.; Dobbelaere, T.; Devloo-Casier, K.; et al. Independent Tuning of Size and Coverage of Supported Pt Nanoparticles Using Atomic Layer Deposition. *Nat. Commun.* **2017**, *8*, 1074.

(37) Mackus, A. J. M.; Leick, N.; Baker, L.; Kessels, W. M. M. Catalytic Combustion and Dehydrogenation Reactions during Atomic Layer Deposition of Platinum. *Chem. Mater.* **2012**, *24*, 1752–1761.

(38) Mackus, A. J. M.; Verheijen, M. A.; Leick, N.; Bol, A. A.; Kessels, W. M. M. Influence of Oxygen Exposure on the Nucleation of Platinum Atomic Layer Deposition: Consequences for Film Growth, Nanopatterning, and Nanoparticle Synthesis. *Chem. Mater.* **2013**, *25*, 1905–1911.

(39) Yuan, H.; Luo, B.; Yu, D.; Cheng, A.; Campbell, S. A.; Gladfelter, W. L. Atomic Layer Deposition of Al-Doped ZnO Films Using Ozone as the Oxygen Source: A Comparison of Two Methods to Deliver Aluminum. *J. Vac. Sci. Technol. A Vacuum, Surfaces, Film.* **2012**, *30*, 01A138.

(40) Na, J.-S.; Peng, Q.; Scarel, G.; Parsons, G. N. Role of Gas Doping Sequence in Surface Reactions and Dopant Incorporation during Atomic Layer Deposition of Al-Doped ZnO. *Chem. Mater.* **2009**, *21*, 5585–5593.

(41) Luka, G.; Wachnicki, L.; Witkowski, B. S.; Krajewski, T. A.; Jakiela, R.; Guziewicz, E.; Godlewski, M. The Uniformity of Al Distribution in Aluminum-Doped Zinc Oxide Films Grown by Atomic Layer Deposition. *Mater. Sci. Eng. B* **2011**, *176*, 237–241.

(42) Kim, S. K.; Choi, G. J.; Kim, J. H.; Hwang, C. S. Growth Behavior of Al-Doped TiO_2 Thin Films by Atomic Layer Deposition. *Chem. Mater.* **2008**, *20*, 3723–3727.

(43) Babar, S.; Mane, A. U.; Yanguas-Gil, A.; Mohimi, E.; Haasch, R. T.; Elam, J. W. $W:Al_2O_3$ Nanocomposite Thin Films with Tunable Optical Properties Prepared by Atomic Layer Deposition. *J. Phys. Chem. C* **2016**, *120*, 14681–14689.

(44) Mane, A. U.; Elam, J. W. Atomic Layer Deposition of $W:Al_2O_3$ Nanocomposite Films with Tunable Resistivity. *Chem. Vap. Depos.* **2013**, *19*, 186–193.

(45) Xie, Q.; Jiang, Y.-L.; Detavernier, C.; Deduytsche, D.; Van Meirhaeghe, R. L.; Ru, G.-P.; Li, B.-Z.; Qu, X.-P. Atomic Layer Deposition of TiO_2 from Tetrakis-Dimethyl-Amido Titanium or Ti Isopropoxide Precursors and H_2O. *J. Appl. Phys.* **2007**, *102*, 083521.

(46) Musschoot, J.; Xie, Q.; Deduytsche, D.; Van den Berghe, S.; Van Meirhaeghe, R. L.; Detavernier, C. Atomic Layer Deposition of Titanium Nitride from TDMAT Precursor. *Microelectron. Eng.* **2009**, *86*, 72–77.

(47) Ramachandran, R. K.; Dendooven, J.; Poelman, H.; Detavernier, C. Low Temperature Atomic Layer Deposition of Crystalline In_2O_3 Films. *J. Phys. Chem. C* **2015**, *119*, 11786–11791.

(48) Aaltonen, T.; Ritala, M.; Sajavaara, T.; Keinonen, J.; Leskela, M. Atomic Layer Deposition of Platinum Thin Films. *Chem. Mater.* **2003**, *15*, 1924–1928.

(49) Ramachandran, R. K.; Dendooven, J.; Filez, M.; Galvita, V. V.; Poelman, H.; Solano, E.; Minjauw, M. M.; Devloo-Casier, K.; Fonda, E.; Hermida-Merino, D.; et al. Atomic Layer Deposition Route To Tailor Nanoalloys of Noble and Non-Noble Metals. *ACS Nano* **2016**, *10*, 8770–8777.

(50) Knaepen, W.; Detavernier, C.; Van Meirhaeghe, R. L.; Jordan Sweet, J.; Lavoie, C. In-Situ X-Ray Diffraction Study of Metal Induced Crystallization of Amorphous Silicon. *Thin Solid Films* **2008**, *516*, 4946–4952.

(51) Knaepen, W.; Gaudet, S.; Detavernier, C.; Van Meirhaeghe, R. L.; Sweet, J. J.; Lavoie, C. In Situ X-Ray Diffraction Study of Metal Induced Crystallization of Amorphous Germanium. *J. Appl. Phys.* **2009**, *105*, 083532.

(52) Koningsberger, D. C.; Mojet, B. L.; van Dorssen, G. E.; Ramaker, D. E. XAFS Spectroscopy; Fundamental Principles

and Data Analysis. *Top. Catal.* **2000**, *10*, 143–155.

(53)   Schlossmacher, P.; Klenov, D. O.; Freitag, B.; von Harrach, H. S. Enhanced Detection Sensitivity with a New Windowless XEDS System for AEM Based on Silicon Drift Detector Technology. *Micros. Today* **2010**, *18*, 14–20.

(54)   Lu, J.; Liu, B.; Guisinger, N. P.; Stair, P. C.; Greeley, J. P.; Elam, J. W. First-Principles Predictions and in Situ Experimental Validation of Alumina Atomic Layer Deposition on Metal Surfaces. *Chem. Mater.* **2014**, *26*, 6752–6761.

(55)   Hübner, M.; Koziej, D.; Bauer, M.; Barsan, N.; Kvashnina, K.; Rossell, M. D.; Weimar, U.; Grunwaldt, J. D. The Structure and Behavior of Platinum in SnO_2-Based Sensors under Working Conditions. *Angew. Chemie - Int. Ed.* **2011**, *50*, 2841–2844.

(56)   Solano, E.; Dendooven, J.; Ramachandran, R. K.; Van de Kerckhove, K.; Dobbelaere, T.; Hermida-Merino, D.; Detavernier, C. Key Role of Surface Oxidation and Reduction Processes in the Coarsening of Pt Nanoparticles. *Nanoscale* **2017**, *9*, 13159–13170.

(57)   Lu, J.; Elam, J. W.; Stair, P. C. Atomic Layer Deposition—Sequential Self-Limiting Surface Reactions for Advanced Catalyst "Bottom-up" Synthesis. *Surf. Sci. Rep.* **2016**, *71*, 410–472.

(58)   Lu, J.; Low, K.-B.; Lei, Y.; Libera, J. A.; Nicholls, A.; Stair, P. C.; Elam, J. W. Toward Atomically-Precise Synthesis of Supported Bimetallic Nanoparticles Using Atomic Layer Deposition. *Nat. Commun.* **2014**, *5*, 3264.

(59)   Weber, M. J.; MacKus, A. J. M.; Verheijen, M. A.; Van Der Marel, C.; Kessels, W. M. M. Supported Core/Shell Bimetallic Nanoparticles Synthesis by Atomic Layer Deposition. *Chem. Mater.* **2012**, *24*, 2973–2977.

(60)   Elam, J. W.; Zinovev, A.; Han, C. Y.; Wang, H. H.; Welp, U.; Hryn, J. N.; Pellin, M. J. Atomic Layer Deposition of Palladium Films on Al_2O_3 Surfaces. *Thin Solid Films* **2006**, *515*, 1664–1673.

(61)   Minjauw, M. M.; Solano, E.; Sree, S. P.; Asapu, R.; Van Daele, M.; Ramachandran, R. K.; Heremans, G.; Verbruggen, S. W.; Lenaerts, S.; Martens, J. A.; et al. Plasma-Enhanced Atomic Layer Deposition of Silver Using $Ag(Fod)(PEt_3)$ and NH_3-Plasma. *Chem. Mater.* **2017**, *29*, 7114–7121.

(62)   Griffiths, M. B. E.; Pallister, P. J.; Mandia, D. J.; Barry, S. T.

Atomic Layer Deposition of Gold Metal. *Chem. Mater.* **2016**, *28*, 44–46.

(63)   Van Daele, M.; Griffiths, M. B. E.; Raza, A.; Minjauw, M. M.; Solano, E.; Feng, J.; Ramachandran, R. K.; Clemmen, S.; Baets, R.; Barry, S.; et al. Plasma-Enhanced Atomic Layer Deposition of Nanostructured Gold near Room Temperature. *ACS Appl. Mater. Interfaces* **2019**, 11, 37229-37238.

(64)   Aaltonen, T.; Rahtu, A.; Ritala, M.; Leskelä, M. Reaction Mechanism Studies on Atomic Layer Deposition of Ruthenium and Platinum. *Electrochem. Solid-State Lett.* **2003**, *6*, C130.

(65)   Kessels, W. M. M.; Knoops, H. C. M.; Dielissen, S. A. F.; MacKus, A. J. M.; Van De Sanden, M. C. M. Surface Reactions during Atomic Layer Deposition of Pt Derived from Gas Phase Infrared Spectroscopy. *Appl. Phys. Lett.* **2009**, *95*, 1–4.

(66)   Van Daele, M.; Detavernier, C.; Dendooven, J. Surface Species during ALD of Platinum Observed with: In Situ Reflection IR Spectroscopy. *Phys. Chem. Chem. Phys.* **2018**, *20*, 25343–25356.

(67)   Lee, H.; Bent, S. F. Microstructure-Dependent Nucleation in Atomic Layer Deposition of Pt on TiO_2. *Chem. Mater.* **2012**, *24*, 279–286.

(68)   Liu, C.; Wang, C.-C.; Kei, C.-C.; Hsueh, Y.-C.; Perng, T.-P. Atomic Layer Deposition of Platinum Nanoparticles on Carbon Nanotubes for Application in Proton-Exchange Membrane Fuel Cells. *Small* **2009**, *5*, 1535–1538.

(69)   Novak, S.; Lee, B.; Yang, X.; Misra, V. Platinum Nanoparticles Grown by Atomic Layer Deposition for Charge Storage Memory Applications. *J. Electrochem. Soc.* **2010**, *157*, H589.

(70)   Yanguas-Gil, A.; Peterson, K. E.; Elam, J. W. Controlled Dopant Distribution and Higher Doping Efficiencies by Surface-Functionalized Atomic Layer Deposition. *Chem. Mater.* **2011**, *23*, 4295–4297.

(71)   Christensen, S. T.; Elam, J. W.; Lee, B.; Feng, Z.; Bedzyk, M. J.; Hersam, M. C. Nanoscale Structure and Morphology of Atomic Layer Deposition Platinum on SrTiO3 (001). *Chem. Mater.* **2009**, *21*, 516–521.

For Table of Contents Only